Orientation-independent differential interference contrast microscopy and its combination with an orientation-independent polarization system

Michael Shribak
Marine Biological Laboratory
7 MBL Street
Woods Hole, Massachusetts 02543

James LaFountain
University at Buffalo
Department of Biological Sciences
657 Cooke Hall
Buffalo, New York 14260

David Biggs
AutoQuant Imaging, Inc.
105 Jordan Road
Troy, New York 12180

Shinya Inouè
Marine Biological Laboratory
7 MBL Street
Woods Hole, Massachusetts 02543

Abstract. We describe a combined orientation-independent differential interference contrast OI-DIC and polarization microscope and its biological applications. Several conventional DIC images were recorded with the specimen oriented in different directions followed by digital alignment and processing of the images. Then the obtained images are used for computation of the phase gradient magnitude and azimuth distribution and, further, the phase image. The OI-DIC images were obtained using optics having numerical aperture (NA) 1.4, thus achieving a level of resolution not previously achieved with phase contrast or interference microscope. The combined system yields two complementary phase images of thin optical sections of the specimen: distribution of refractive index and distribution of birefringence due to anisotropy of the cell structure. For instance, in a live dividing cell, the OI-DIC image clearly shows the detailed shape of the chromosomes, while the polarization image quantitatively depicts the distribution of birefringent microtubules in the spindle, both without any need for staining or other modifications of the cell. We present pseudo-color combined images of a crane fly spermatocyte at diakinesis and metaphase of meiosis I. Those images provide clear evidence that the proposed technique can reveal fine architecture and molecular organization in live cells without perturbation associated with staining or fluorescent labeling. [DOI: 10.1117/1.2837406]

Keywords: differential interference contrast (DIC) microscopy; phase microscopy; polarized microscopy; optical path gradient; dry mass; birefringence.

Paper 07156R received Apr. 28, 2007; revised manuscript received Oct. 1, 2007; accepted for publication Oct. 23, 2007; published online Feb. 12, 2008. This paper is a revision of a paper presented at the SPIE conference on Image, Manipulation, and Analysis of Biomolecules, Cells, and Tissues V, Jan. 2007, San Jose, Calif. The paper presented there appears (unrefereed) in SPIE Proceedings Vol. 6441.

1 Introduction

Differential interference contrast (DIC) microscopy is widely used to observe structure and motion in unstained living cells and isolated organelles. The technique produces a monochromatic shadow-cast image of optical path (dry mass) gradient with a transparent specimen. Those regions of the specimen where the optical paths increase along a reference direction appear brighter (or darker), while regions where the path differences decrease appear in opposite contrast. Where there are steep gradients of optical path, image contrast is significantly increased. Another important feature of the DIC technique is that it permits effective optical sectioning, employing high numerical aperture (NA) objectives together with high NA condenser illumination. With conventional DIC, the two-dimensional (2-D) distribution of optical path gradients along the shear direction generates image contrast that is not symmetrical and varies proportionally with the cosine of the angle made by the azimuth of the object and the direction of wavefront shear.

Polarized light microscopy reveals structural anisotropy due to form birefringence, intrinsic birefringence, stress birefringence, etc. Thus, polarization microscopy data can be considered as complementary to DIC results. The DIC and polarization techniques are able to image a thin optical section of specimen under investigation. Capacity for efficient optical sectioning of thick objects is one of the most important advantages of DIC microscopy in biology and medicine.[1,2] It was shown[3] that the thickness of the optical sections, with illumination at 546 nm and a 0.95 NA objective lens, can be as little as 0.25 to 0.3 μm for DIC and 0.15 to 0.2 μm for rectified polarization microscopy, Using formulas from Ref. 4, one can find that, under the same conditions, a theoretical depth of field of a conventional brightfield microscope is 0.8 μm. Both DIC and polarization methods, however, have the same shortcomings: they require the proper orientation of

Address all correspondence to Michael Shribak, MS 119, Marine Biological Laboratory, 7 MBL Street, Woods Hole, MA 02543; Tel: 508–289–7242; E-mail: mshribak@mbl.edu

1083-3668/2008/13(1)/014011/10/$25.00 © 2008 SPIE

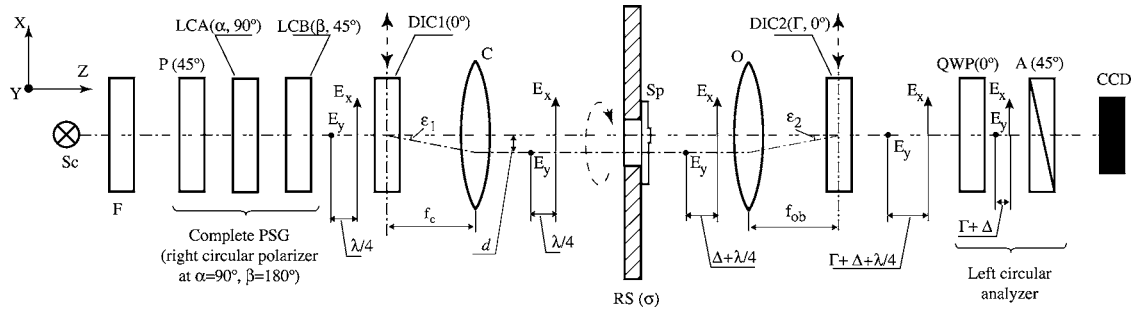

Fig. 1 Scheme of a microscope setup for combined orientation-independent DIC and polarization imaging: Sc, light source; F, bandpass filter; P (45 deg), polarizer at 45-deg azimuth; LCA (α, 90 deg) and LCB (β, 45 deg), liquid crystal variable retarders with retardances α and β at azimuths 90 deg and 45 deg correspondingly; DIC1 (0 deg) and DIC2 (0 deg, Γ), removable Nomarski prisms at 0-deg azimuth (the second prism introduces bias Γ); C, condenser lens; RS (σ), rotatable stage at azimuth σ; Sp, specimen under investigation; O, objective lens; QWP (0 deg), quarter-wave plate at azimuth 0 deg; A (45 deg), linear analyzer at azimuth 45 deg; CCD, imaging detector (CCD camera); XYZ, Cartesian coordinate system. The linear polarizer and two variable retarders form a complete polarization state generator (PSG). The quarter-wave plate and linear analyzer form a left circular analyzer.

a specimen in relation to the optical system in order to achieve best results.

2 Description of Microscope Setup

2.1 *Optical Scheme of Microscope for Combined Orientation-Independent DIC and Polarization Imaging*

A regular research-grade microscope equipped with DIC prisms, polarization state generator (or compensator), circular analyzer, and precision rotatable stage can be employed for obtaining orientation-independent DIC (OI-DIC) and polarization images. Figure 1 illustrates the optical setup that we used. The setup was implemented on an upright microscope Microphot SA (Nikon, Melville, New York, http://www.nikoninstruments.com). The microscope consists of a light source Sc, bandpass filter F, condenser and objective lenses C and O correspondingly, rotatable stage RS, a pair of removable Nomarski prisms DIC1 and DIC2, left circular analyzer, and CCD camera Retiga EXi Fast (QImaging, Surrey, British Columbia, Canada, http://www.qimaging.com), which is connected to a computer. Sp is a specimen under investigation. As a light source, we used a high-pressure mercury arc lamp followed by an Ellis fiber-optic light scrambler (Technical Video, Port Townsend, Washington, http://www.technicalvideo.com). The bandpass interference filter with central wavelength 546 nm and 30-nm full width at half maximum (Chroma Technology, Rockingham, Vermont, http://www.chroma.com) selected the bright green mercury line for illumination.

For description of the setup, we use the right-handed Cartesian coordinate system xyz. The z axis is parallel to the microscope axis toward the beam propagation. The x axis is parallel to the shear direction of the prism DIC1. The orientations of the retarders in the x-y plane are defined by their slow axis. The orientations of the linear polars are determined by their electric vector transmittance axis. The angle is positive if measured counterclockwise and negative if measured clockwise from the x axis, when one is looking "into the beam."

Two liquid crystal variable retarders LCA and LCB together with linear polarizer P (CRi, Inc., Woburn, Massachusetts, http://www.cri-inc.com) form a complete polarization state generator (PSG),[5] which is also called a universal compensator.[6] The polarizer P is oriented at 45 deg. The variable retarders LCA and LCB are oriented at 90 deg and 45 deg, accordingly. This arrangement, which can produce any light polarization, was proposed by Yamaguchi and Hasunuma in 1967.[7,8] The variable retarders LCA and LCB introduce retardances α and β, correspondingly. The basic setting of the retarders is α=90 deg and β=180 deg. In this case, the PSG creates a right circular polarized beam, where the E_x component leaves behind the E_y component on $\lambda/4$ distance, where λ is wavelength. The quarter-wave plate QWP with orientation 0 deg and linear analyzer A with orientation 45 deg construct a left circular analyzer. We used a left circular analyzer made of a laminated polymer achromatic wave plate and polarization film (Bolder Vision Optics, Boulder, Colorado, http://www.boldervision.com).

The complete polarization state generator (PSG), left or right circular analyzer, and CCD camera with computer are employed for obtaining images of 2-D birefringence distribution.[6,9] It is possible also to use other kinds of PSG, such as rotatable elliptical polarizer,[10] rotatable linear polarizer,[11] or combination of liquid crystal variable retarders LCA and LCB with orientation angles 22.5 deg and 67.5 deg,[12] etc. The prisms DIC1 and DIC2 are taken out during the capturing of raw polarization images. A brief description of algorithms for obtaining orientation-independent polarization images is given in Sec. 2.3.

In order to switch to the DIC mode, the prisms must be moved back into the beam, as shown in Fig. 1. The polarization state generator is in the basic setting to create the right circular polarized illumination beam.

The prism DIC1 splits the input beam angularly along the x axis into two orthogonally polarized beams with components E_x and E_y. The axis of the first beam with component E_x is parallel to the z axis. The second beam is deviated on a small angle ε_1. The component intensities are the same, but there is a quarter-wave optical path difference $\lambda/4$ between them because the input beam is circularly polarized. The condenser C makes the beam axes parallel with a small shear d. Then the objective lens O joins the beam axes in the back

focal plane. The second prism DIC2 introduces an opposite small angular deviation ε_2 into the second beam with component E_x. The angles ε_1 and ε_2 are connected with the focal distances of the condenser and objective lenses f_c and f_{ob} and the shear amount d by the following formula:

$$f_c\varepsilon_1 = f_{ob}\varepsilon_2 = d. \tag{1}$$

Thus, the two orthogonally polarized beams are recombined into one beam. The second prism adds also a bias Γ in order to increase sensitivity. The quarter-wave plate QWP of the left circular analyzer introduces an optical path difference of $-\lambda/4$ between the components E_x and E_y, which compensates the initial path difference $\lambda/4$ due to the right circular polarization of the input beam. The analyzer A reduces polarizations of the components E_x and E_y in one plane at 45 deg azimuth, so the beams can interfere. This optical configuration creates a polarizing shearing interferometer, by which one visualizes phase nonuniformity of the specimen. The contrast of a regular DIC image also depends on the orientation of the specimen under investigation relative to the shear direction σ and the amount of bias Γ. The angle σ can be changed by a turn of the rotation stage RS.

We captured two pairs of regular DIC images at orientations of the stage $\sigma=0$ deg and $\sigma=90$ deg. In each pair, the images were taken with small biases having the same magnitude and opposite signs. The computer then rotated off-line the second image pair on −90 deg and aligned one with the first image pair. The four images are processed further to get the OI-DIC image. The corresponding processing algorithm is briefly described in the next section.

2.2 *Algorithm for Orientation-Independent DIC Imaging*

Recently, we proposed a DIC microscopy technique that records phase gradients within microscopic specimens independently of their orientation.[13,14] For description of the specimen under investigation, we use a local Cartesian coordinate system $x'y'$, which is connected with the rotatable stage RS. If the stage orientation $\sigma=0$ deg, then the x' axis coincides with the x axis of the main coordinate system. In case of $\sigma=90$ deg, the y' axis coincides with the x axis. A DIC image can be modeled as the superposition of one image over an identical copy that is displaced along the x axis by a shear amount d and phase shifted by bias Γ. The intensity distribution in the DIC image $I^{DIC}(x',y')$ can be described by the following formula:

$$I^{DIC}(x',y') = \frac{1}{2}\tilde{I}(x,y)\left[1 - \cos\left(\frac{2\pi}{\lambda}\{\Gamma + d\cdot\gamma(x',y')\cos[\theta(x',y')-\sigma]\}\right)\right], \tag{2}$$

where $\tilde{I}(x,y)$ is the intensity of the illumination beam before prism DIC1, $\gamma(x',y')$ and $\theta(x',y')$ are the gradient magnitude and azimuth, and λ is the wavelength.

Here, we assume that the intensity of each interfering imaging beam after the analyzer A equals $\frac{1}{4}$ of intensity $\tilde{I}(x,y)$, retardance of the specimen and depolarization caused by the optical components are small and can be neglected, polarizer P and analyzer A are ideal, and the ambient light is absent.

If the product $d\gamma$ is small ($d\gamma \ll \lambda/2\pi$), Eq. (2) can be reduced to sum of two terms:

$$I^{DIC}(x',y') = K + L\cos[\theta(x',y') - \sigma], \tag{3}$$

where

$$K = \tilde{I}(x,y)\sin^2\left(\frac{\pi}{\lambda}\Gamma\right) \quad \text{and}$$

$$L = \frac{\pi}{\lambda}\tilde{I}(x,y)\cdot d\cdot\gamma(x',y')\sin\left(\frac{2\pi}{\lambda}\Gamma\right).$$

The 2-D distribution of magnitude and azimuth γ and θ can be found by taking two pairs of raw DIC images at specimen orientations $\sigma=0$ deg and $\sigma=90$ deg with positive and negative biases $\pm\Gamma$. In the first case, $\sigma=0$ deg, the axes of the local specimen coordinate system coincide with the microscope coordinate system ($x'=x, y'=y$), and the shear is directed along the x' axis. In the second case, the coordinate systems are relatively turned on 90 deg ($x'=-y, y'=x$), and the shear is directed along y' axis. The CCD camera captures the first image pair $I_1^{DIC}(x,y)$ and $I_2^{DIC}(x,y)$ described by the next equation:

$$I_{1,2}^{DIC}(x,y) = K \pm L\cdot\cos[\theta(x,y)]. \tag{4a}$$

Then the camera captures an image pair of the rotated specimen $I_3^{DIC}(-y,x)$ and $I_4^{DIC}(-y,x)$ at $\sigma=90$ deg. After, the computer rotates digitally the second image pair on −90 deg to get the same orientation for all images:

$$I_{3,4}^{DIC}(x,y) = K \pm L\sin[\theta(x,y)]. \tag{4b}$$

The following two equations calculate the gradient magnitude and azimuth distribution of the optical paths in the specimen:

$$\gamma(x,y) = \frac{\lambda}{2\pi\cdot d}\tan\left(\frac{\pi\Gamma}{\lambda}\right)\left[\left(\frac{I_1^{DIC}-I_2^{DIC}}{I_1^{DIC}+I_2^{DIC}}\right)^2 + \left(\frac{I_3^{DIC}-I_4^{DIC}}{I_3^{DIC}+I_4^{DIC}}\right)^2\right]^{1/2},$$

$$\theta(x,y) = \arctan\left(\frac{I_3^{DIC}-I_4^{DIC}}{I_1^{DIC}-I_2^{DIC}}\right). \tag{5}$$

Notice that the algorithm considered here employs ratios between intensities of light that has interacted with the specimen. Therefore, it suppresses contributions of absorption by the specimen, nonuniformity of illumination, etc., which can otherwise deteriorate a DIC image.

Also, after computing the optical path gradient distribution, enhanced regular DIC images can be restored with any shear direction.[14] The enhanced image provides a calculated image for any desired shear direction and bias without the requirement to directly collect an image for that shear direction and bias. Moreover, the enhanced image will have less

noise than a regular DIC image, and it suppresses deterioration of the image due to specimen absorption and illumination nonuniformity.

Optical phase $\Phi(x,y)$ shows the dry mass distribution of a specimen and can be obtained by computing a line integral.[14,15] Also other techniques for phase computation can be used, for instance, iterative computation,[16] noniterative Fourier phase integration,[17] or nonlinear optimization with hierarchical representation,[18] etc. Biggs has developed an iterative deconvolution approach for computation of phase images, based on the same principles as deconvolution techniques normally used to remove out-of-focus haze.[19] When processing DIC data, the point spread function (PSF or h) that describes the image formation process can be approximated[16] using a positive and negative Dirac delta δ function separated by the shear distance d:

$$\sigma = 0 \text{ deg:} \quad h_0(x,y) = \delta\left(x - \frac{d}{2}, y\right) - \delta\left(x + \frac{d}{2}, y\right),$$

$$\sigma = 90 \text{ deg:} \quad h_{90}(x,y) = \delta\left(x, y - \frac{d}{2}\right) - \delta\left(x, y + \frac{d}{2}\right). \quad (6)$$

The processing is assumed to operate on the differential phase data, which can be calculated from the intensity images taken at the shear orientations with 90-deg differences:

$$OPD_0(x,y) = \frac{2\pi}{\lambda} d \cdot \gamma(x,y) \cos\theta(x,y),$$

$$OPD_{90}(x,y) = \frac{2\pi}{\lambda} d \cdot \gamma(x,y) \sin\theta(x,y). \quad (7)$$

Using Eqs. (3) and (4), we can derive the following equations for the differential phase data $OPD_0(x,y)$ and $OPD_{90}(x,y)$:

$$OPD_0 = \frac{L}{K} \tan\left(\frac{\pi\Gamma}{\lambda}\right) \cos\theta(x,y) = \frac{I_1^{DIC} - I_2^{DIC}}{I_1^{DIC} + I_2^{DIC}} \tan\left(\frac{\pi\Gamma}{\lambda}\right),$$

$$OPD_{90} = \frac{L}{K} \tan\left(\frac{\pi\Gamma}{\lambda}\right) \sin\theta(x,y) = \frac{I_3^{DIC} - I_4^{DIC}}{I_3^{DIC} + I_4^{DIC}} \tan\left(\frac{\pi\Gamma}{\lambda}\right). \quad (8)$$

The two resulting data sets have orthogonal shear directions (and orthogonal PSFs) but a common underlying phase object. As mentioned earlier, any absorption variations have been eliminated by calculating the ratios of image intensities. The observed differential phase is simply the true object $\Phi(x,y)$ convolved ($\otimes$) with the PSF, plus a noise component $n(x,y)$:

$$OPD(x,y) = \Phi(x,y) \otimes h(x,y) + n(x,y). \quad (9)$$

The true optical path length of the phase object can be reconstructed by forming a least-squares error metric e and using iterative gradient descent optimization with acceleration[20] to estimate a single solution $\hat{\Phi}(x,y)$ that fits both observations:

$$e = \sum_{x,y} |\hat{\Phi}(x,y) \otimes h_0(x,y) - OPD_0(x,y)|^2 + |\hat{\Phi}(x,y) \otimes h_{90}(x,y) - OPD_{90}(x,y)|^2. \quad (10)$$

Typically, 100 iterations are required with gradient descent. Faster convergence could be achieved using conjugate gradients or any other optimization procedure. Depending upon *a priori* knowledge about the true specimen, a penalty term can also be introduced to minimize negative phase values with respect to the background, which can suppress potential reconstruction artifacts. The resolution of the estimated optical path length image can also be improved by taking into account the finite lateral resolution of the microscope and applying a second deconvolution procedure. The 2-D iterative blind deconvolution algorithm that is part of the AutoQuant software package (Media Cybernetics, Bethesda, Maryland) is used to determine the PSF directly from the provided image, and simultaneously improve the resolution of the image. Once the PSF is known, only five iterations are typically required to restore subsequent images.

2.3 *Algorithm for Orientation-Independent Polarization Imaging*

In order to switch to the Pol (polarization) mode, the prisms must to be moved out from the beam. The rotatable stage RS is oriented at $\sigma = 0$ deg. Thus, the specimen coordinate system $x'y'$ is coincident with the microscope coordinate system xy. For obtaining orientation-independent polarization images, we employed the four-frame algorithm proposed by Shribak.[10,21] The algorithm computes 2-D distributions of retardance $\Delta(x,y)$ and slow-axis orientation (azimuth) $\varphi(x,y)$ of the specimen under investigation.

Intensity distribution in a Pol image $I^{Pol}(x,y)$, which is created after the left circular analyzer, can be described by the following formula:

$$I^{Pol}(x,y) = \frac{1}{2}\tilde{I}(x,y)\big[1 + \sin\alpha\cos\beta\cos\Delta(x,y) + \sin\alpha\sin\beta\sin 2\varphi(x,y)\sin\Delta(x,y) + \cos\alpha\cos 2\varphi(x,y)\sin\Delta(x,y)\big], \quad (11)$$

where $\tilde{I}(x,y)$ is the intensity of the illumination beams, and α and β are the retardances introduced by the variable retarders LCA and LCB, correspondingly. Initially, the polarization state generator PSG is in the basic setting: $\alpha = 90$ deg, $\beta = 180$ deg. If the retardances α and β deviate from the nominal on small amounts χ_α and χ_β and the retardance of the specimen under investigation Δ is small, Eq. (11) can be simplified as:

$$I^{Pol}(x,y) = \frac{1}{4}\tilde{I}(x,y)[\chi_\alpha^2 + \chi_\beta^2 + \Delta^2(x,y) + 2\chi_\alpha\Delta(x,y)\cos 2\varphi(x,y) + 2\chi_\beta\Delta(x,y)\sin 2\varphi(x,y)]. \quad (12)$$

Here, we neglect the third power and higher small terms of series expansion.

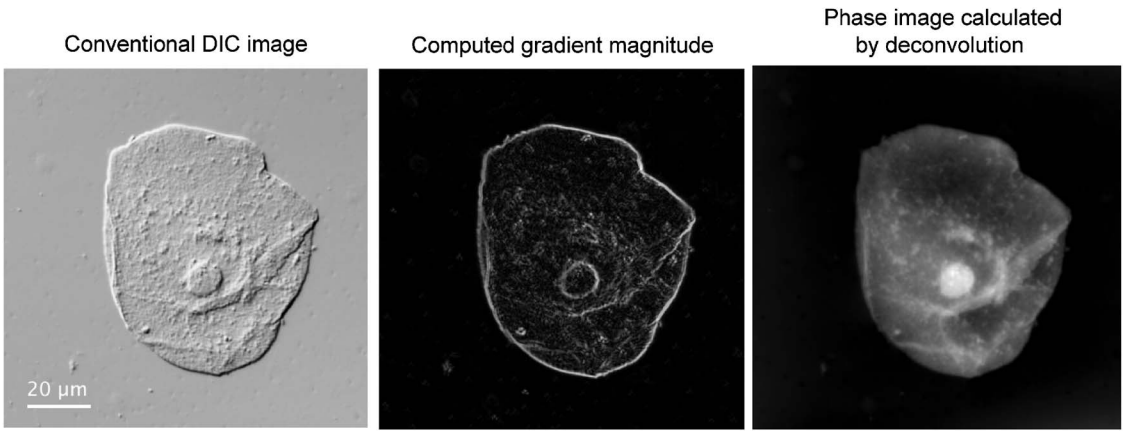

Fig. 2 Conventional and computed orientation-independent DIC images of human cheek squamous epithelial cell.

At first, we record an image pair $I_1^{Pol}(x,y)$ and $I_2^{Pol}(x,y)$ with negative and positive small bias χ applied to nominal retardance of the first variable retarder ($\chi_\alpha = \mp\chi$, $\chi_\beta = 0$ deg):

$$I_{1,2}^{Pol}(x,y) = \frac{1}{4}\tilde{I}(x,y)[\chi^2 + \Delta^2(x,y) \mp 2\chi\Delta(x,y)\cos 2\varphi(x,y)]. \tag{13a}$$

We capture also the second pair of images $I_3^{Pol}(x,y)$ and $I_4^{Pol}(x,y)$ with negative and positive bias χ applied to nominal retardance of the second variable retarder ($\chi_\alpha = 0$ deg, $\chi_\beta = \mp\chi$):

$$I_{3,4}^{Pol}(x,y) = \frac{1}{4}\tilde{I}(x,y)[\chi^2 + \Delta^2(x,y) \mp 2\chi\Delta(x,y)\sin 2\varphi(x,y)]. \tag{13b}$$

Then the following two terms are employed to calculate the distributions of retardance $\Delta(x,y)$ and slow-axis orientation (azimuth) $\varphi(x,y)$:

$$\Delta(x,y) = \frac{M}{[1+(1-M^2)]^{1/2}}\chi,$$

$$\varphi(x,y) = \frac{1}{2}\arctan\left(\frac{I_4^{Pol} - I_3^{Pol}}{I_2^{Pol} - I_1^{Pol}}\right), \tag{14}$$

where

$$M = \left[\left(\frac{I_2^{Pol} - I_1^{Pol}}{I_2^{Pol} + I_1^{Pol}}\right)^2 + \left(\frac{I_4^{Pol} - I_3^{Pol}}{I_4^{Pol} + I_3^{Pol}}\right)^2\right]^{1/2}.$$

Usually, we have $\Delta \ll \chi$. In this case, the formula for computation of the specimen retardance can be simplified as:

$$\Delta(x,y) = \frac{1}{2}M \cdot \chi. \tag{15}$$

3 Examples of Imaging Biological Objects with Orientation-Independent DIC Microscopy

The OI-DIC technique was applied to a variety of biological objects in order to evaluate its applicability to different cytological contexts. The results summarized here demonstrate the broad potential that OI-DIC offers to a wide range of fields where cellular microscopy is employed.

3.1 *OI-DIC Images of Human Cheek Squamous Epithelial Cells*

Human cheek cells are excellent transparent test specimens commonly used for alignment of the microscope for phase contrast and DIC.[2,22] For the preparations used here, a buccal smear of cheek cells was dispersed in a drop of 1× phosphate-buffered saline (Sigma-Aldrich, St. Louis, Missouri, http://www.sigmaaldrich.com) on a 1.5-thick coverslip, which was then inverted onto a clean slide and pressed down to spread the cells into a thin layer. Four conventional DIC images were obtained, as explained in Sec. 2.1. We used the Nikon Microphot-SA microscope equipped with a 20×/0.5 Plan DIC objective lens. Bias of 1/15 wavelength was introduced with a Brace-Koehler compensator.

Figure 2 (left) illustrates one of the captured conventional DIC images. Figure 2 (center) is a grayscale image of gradient magnitude computed from Eq. (5). Here, brightness is linearly proportional to the magnitude. The gradient magnitude image clearly shows the cell and nuclear boundaries independently of orientation. The computed phase is entirely consistent with the structure seen with conventional DIC, but the clarity is significantly improved. Notice also how the large (10-μm diam) optically refractive nucleus appears distinct within the cheek cell cytoplasm in this image.

3.2 *Orientation-Independent DIC Images of Sciara coprophila Polytene X Chromosomes*

Application of OI-DIC to isolated chromosomes is illustrated using giant salivary gland chromosomes from the fungus gnat, *Sciara coprophila*. Salivary glands were obtained from female larvae in Robert's CR medium (87 mM NaCl, 3.2 mM KCl, 1.3 mM $CaCl_2$, 1 mM $MgCl_2$, 10 mM Tris-HCl; pH 7.3)

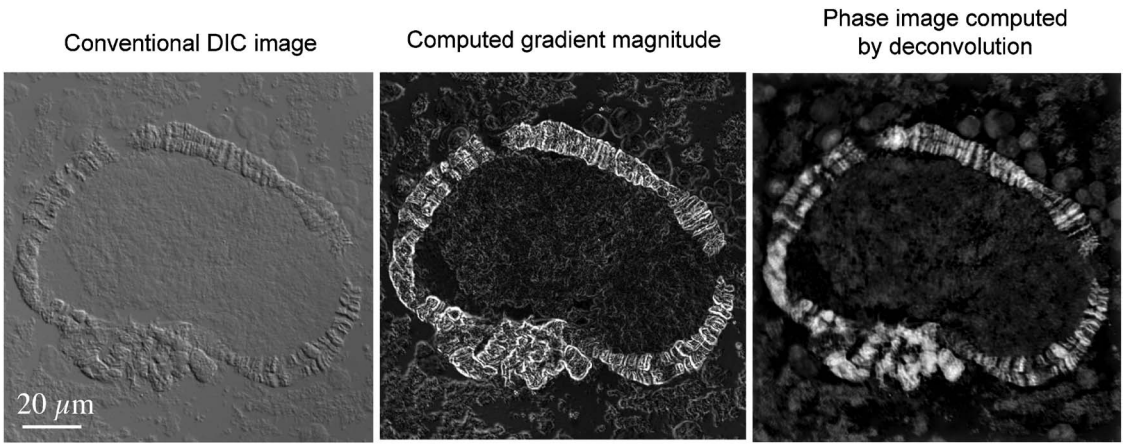

Fig. 3 Conventional and computed orientation-independent DIC images of *Sciara* polytene X chromosomes.

and gently squashed on a coverslip to spread the chromosomes.

Figure 3 shows how the banded appearance of these polytene chromosomes (which result from the recombination and repeated replication of chromosomal DNA) can be imaged in both conventional DIC and gradient magnitude modes. Sites where chromosomal DNA is dispersed ("puffs") are clearly evident. These images were obtained under the same experimental conditions as for the human check cells described in the preceding section, except for microscope lens NA. Here, we used a $40\times/0.7$ Plan DIC objective.

3.3 *OI-DIC Images of Vorticella*

Here, experimental results with biological specimens explored at very high image resolution are presented. The protist *Vorticella convallaria* is especially interesting, as its spasmoneme is among the fastest and most powerful cellular engines known.[23] Figure 4 shows conventional DIC, gradient magnitude, and phase images of an anesthetized *Vorticella* cell with a contracted stalk. The cell was induced to contract by the addition of dibucaine hydrochloride D0638 (Sigma-Aldrich, St. Louis, Missouri, http://www.sigmaaldrich.com), a local anesthetic that demonstrates many other cellular effects secondary to its anesthetic capabilities. In order to obtain the OI-DIC images, four conventional DIC images were made, as described earlier. The images were then digitally aligned and processed to obtain those displayed in the center and right panels of Fig. 4. The setup was a Nikon Microphot-SA microscope equipped with a $60\times/1.4$ NA oil immersion objective lens and a Universal Achromatic-Aplanat condenser with the same NA at wavelength 546 nm.

In the phase image, the vacuoles (with their lower dry mass) clearly stand out from organelles with higher optical density. The spasmoneme has obviously contracted within the stalk, as seen by its increased concentration away from the cell body. The contracted spasmoneme is 4.3-μm thick, and it tightly fills the sheath. Also some of the structures within the oral groove—the basal bodies near the "mouth" of the cell (farthest from the stalk connection) and cilia (within the middle-left portion of the cell body)—stand out distinctly. Many detached cilia are evident floating in the area surrounding the cell, apparently detached from the cell in response to the dibucaine treatment used to anesthetize the cell.

Deserving emphasis is the fact that images with such high fidelity and resolution, and reflecting the true distribution of optical paths (dry mass), cannot be obtained with conventional phase contrast or interference contrast techniques. The former introduces a halo around regions with high optical

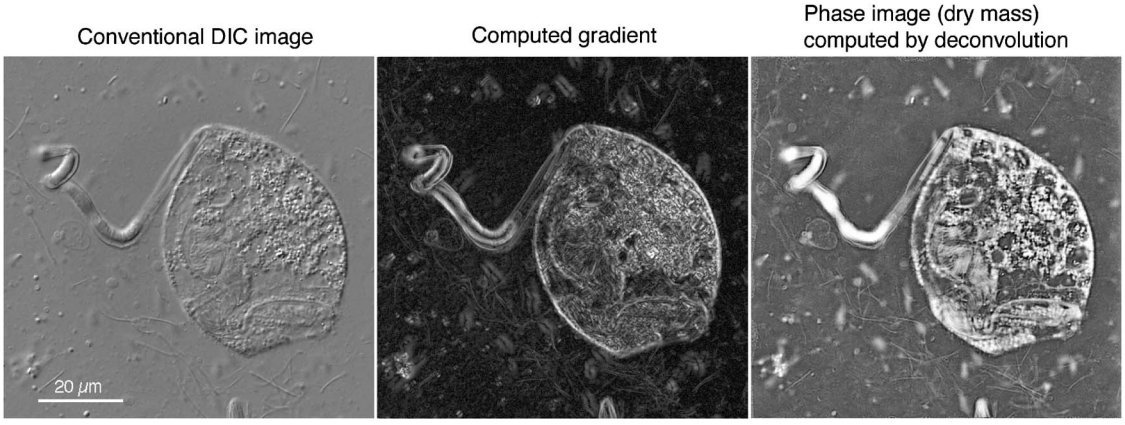

Fig. 4 Conventional DIC image and computed orientation-independent DIC images of *Vorticella*.

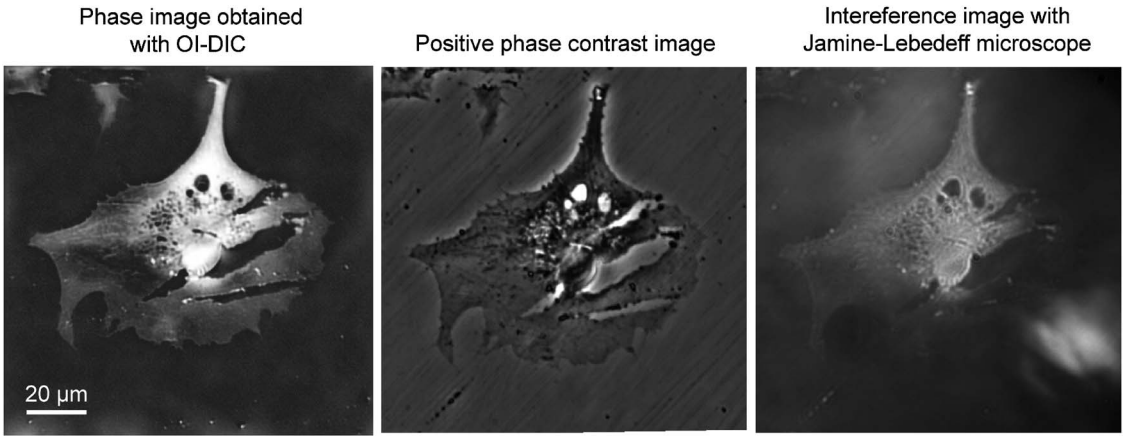

Fig. 5 Computed OI-DIC image positive phase contrast image, and interference image of bovine pulmonary artery endothelial cell.

path differences in the specimen, by suppressing low-frequency details because of spatial filtration by the phase annulus. Interference microscopy, on the other hand, cannot be used with high NA lenses, thus preventing the achievement of high image resolution. Our new approach improves upon the resolution, image quality, and fidelity of DIC, phase contrast, and interference microscopy and finally allows acquisition of images that depict the true optical path difference at the highest resolution of well-corrected microscope lenses. These results demonstrate that the proposed DIC technique can successfully image and measure phase gradients of transparent specimens, such as those of biomedical interest, independent of the directions of the gradient, and minimally influenced by specimen absorption.

3.4 *Comparison of OI-DIC, Phase Contrast, and Interference Images of Fixed Bovine Pulmonary Artery Endothelial Cells*

Our first attempts at imaging a biological specimen with the OI-DIC technique were done using a specimen slide containing fixed and stained bovine pulmonary artery endothelial cells that are commercially available from Invitrogen (Carlsbad, California, slide product number F14780). These cells were chosen because of their distinct shape. In an earlier report,[14] we described the improvements made by OI-DIC in the imaging of these cells in comparison to images made with conventional DIC. Here, we present results obtained with phase contrast and interferometric microscopy techniques.

Figure 5 demonstrates a phase image obtained with OI-DIC technique (left), a conventional phase contrast image (center), and an interference image of the cell (right). The images show the dry mass distribution of the cell under investigation.

In order to obtain the OI-DIC image, we employed a Nikon $20\times/0.75$ NA objective and a Nikon Universal Achromatic-Aplanat 1.4 NA condenser stopped down to match the objective NA. Four conventional DIC images were collected and aligned as described earlier. Then the phase image was computed via iterative deconvolution. The OI-DIC phase images clearly reveal the refractive boundaries and detailed structures of the cell. The image brightness is linearly proportional to the dry mass.

The phase contrast image was obtained with a Nikon Microphot-SA microscope equipped with an ePlan $40\times/0.65$ phase objective lens containing a positive phase ring. With this phase ring, specimens having a higher refractive index than the surrounding medium appear dark on a neutral gray background, while those specimens that have a lower refractive index than the bathing medium appear brighter than the gray background. The phase image has two artifacts:

- A phase halo that is a diffuse ring with an intensity opposite that of the specimen and surrounding the specimen. In positive phase contrast, a dark specimen will have a bright halo on a light background. In negative phase contrast, a light specimen will have a dark halo on a darker background.
- A shading off effect that occurs within the specimen itself. If the specimen is dark, there will be a central bright region that shades off into the dark body of the specimen. If the specimen is light there will be a central dark region that shades off into the light body of the specimen.

The interference image was obtained with a Jamin-Lebedeff microscope equipped with a Pol-Int II $40\times/0.65$ objective lens and a Senarmont compensator. The objective lens introduces 180-μm displacement between the probe and reference beams in the object plane. The specimen under investigation does not have an empty space around the cell for the reference beam. Therefore, the interference image contains blurred areas from the surrounding structure. The image brightness depends on the dry mass nonlinearly.

4 Combined Orientation-Independent DIC and Polarization Images of Meiosis in Crane Fly Spermatocytes

OI-DIC and orientation-independent polarization techniques yield two complementary images: one showing dry mass distribution (which is proportional to refractive index) and the other showing distribution of birefringence (due to structural or internal anisotropy). For example, in a live dividing cell, the DIC image will clearly show the detailed shapes of the chromosomes, while the polarization image will quantitatively depict the distribution of the birefringent microtubules in the spindle, both without any need for staining or other modifications of the cell.

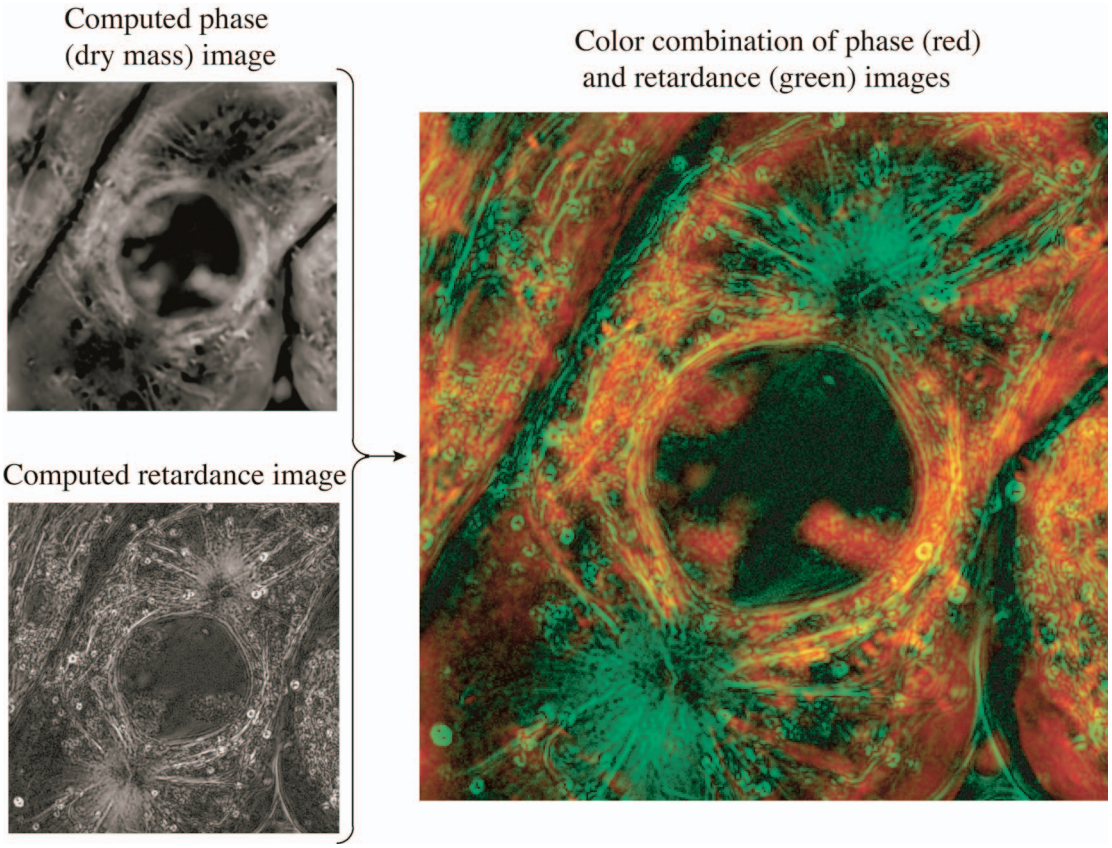

Fig. 6 Diakinesis of meiosis I in a crane fly spermatocyte.

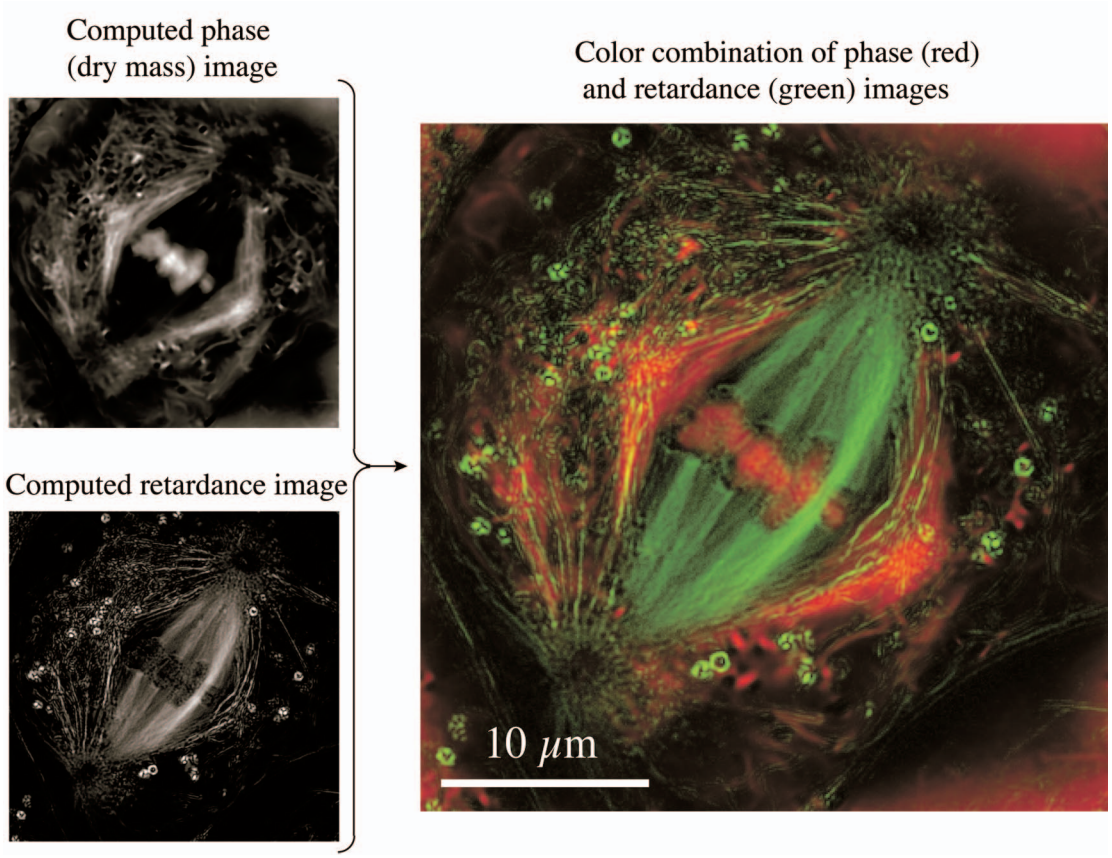

Fig. 7 Metaphase of meiosis I in a crane fly spermatocyte.

Here pseudo-color examples of OI-DIC and OI-Pol images of spermatocytes from the crane fly, *Nephrotoma suturalis,* during meiosis I are presented. The setup was a Nikon Microphot-SA microscope equipped with a 60×/1.4 NA oil immersion objective and a Universal Achromatic-Aplanat condenser with the same NA at wavelength 546 nm. The changing of the bias and rotating of the shear direction during DIC image acquisition were done manually. Also, in order to switch between polarization and DIC imaging modes, the pair of liquid crystal wave plates was replaced with DIC prisms (see Fig. 1). Unfortunately, these mechanical manipulations took some time, thus resulting in significant sacrifice of temporal resolution during the test, as discussed below.

Summary of protocol. Four raw polarization mode images were acquired with intervals of 0.03 s (total acquisition time 0.12 s). Switching from the polarization mode to the DIC mode and adjustment of the bias took 2 min, 30 s, and then three DIC mode images with inverse biases and with zero bias were made with intervals of 5 s, followed by rotation of the microscope stage for 28 s, then another set of three DIC mode images with intervals of 5 s. The total time of DIC image acquisition was 10+28+10=48 s.

Figures 6 and 7 are images of the same spermatocyte during meiosis I first recorded during diakinesis (Fig. 6) and then later at metaphase (Fig. 7). They contain computed phase (dry mass) mode (left-top), computed retardance mode (left-bottom), and color combination of the dry mass and retardance modes (right), in which red and green colors correspond to dry mass distribution and retardance, respectively.

Those figures illustrate morphological structures, such as the chromosomes, that are especially prominent in the phase mode image. Other features, such as the birefringent spindle fibers (actually bundles of microtubles), exhibit much better contrast in the retardance mode.

The phase image [Fig. 7(c)] reveals a dry mass difference between the kinetochore (K-) fibers and the domains of the spindle that surround them. Most notable are the K-fibers extending toward the bottom pole. In the retardance image, they are clearly resolved as birefringent structures, whereas in the gradient image, they appear as weakly refractile structures, just slightly brighter than the surround. The image is very black, but the K-fibers are clearly evident as slightly brighter (whiter) than their surround. Thus, those metaphase K-fibers provide a good test object for gradient and phase mode imaging, due to their slightly greater optical density than their surround.

But the K-fibers also raise a problem. They show visible structures in conventional DIC mode [Fig. 7(a)], which are almost absent in the gradient and phase images. This aberration likely is caused by movement(s) occurring during the time interval between subsequent regular DIC images.

This explanation is further supported by Biggs's observation that when he deconvolved the DIC images, the first set appeared to be very different from the second set, likely a consequence of a longer time interval between the sets than the time between frames within a set, as described earlier. When the proposed setup diagrammed in our patent application[13] will be implemented, the time interval for raw DIC image acquisition is expected to be 0.3 s, and thus such artifacts due to movement of (or within) the specimen will be minimized, if not fully abolished.

Figures 6 and 7 provide clear evidence of our notion that the proposed technique can reveal the architecture (morphology) of live cells without staining and fluorescent labeling. The phase image acquired in this fashion yields the true distribution of optical path differences using 1.4 NA optics, a feat not previously achieved with interference microscope.

5 Conclusion

This report presents the theoretical basis for OI-DIC microscopy. The new approach allows precise analyses of organelle morphology, motility, shape changes, as well as dry mass distribution, importantly within unstained living cells. Using conventional DIC optics and a microscope equipped with a precision rotating stage as a prototype, confirmation of the theoretical principles of the proposed technique has been achieved. Through implementation of the algorithms described in this report into the construction of a new OI-DIC microscope, it should be possible with the next-generation instrument to produce digital OI-DIC images in a fraction of a second, thus overcoming limits on temporal resolution that exist at present with the prototype. Combined with the OI-Pol system, the OI-DIC microscope should become a powerful new instrument for the study of submicroscopic and molecular events that require concurrent analyses of organelle movements and anisotropy of motile filamentous structures.

Acknowledgments

We are grateful to Dr. Rudolf Oldenbourg of MBL for his encouragement and support. We thank our collaborator Danielle France-Cook, Whitehead Institute, MTI, and Dr. Brigitte de Saint Phalle, MBL, for generously providing samples. We thank Grant B. Harris of MBL for software development employed in the OI-Pol experiments. This research is funded by the National Institute of Health Grant No. R01 EB005710 awarded to M. Shribak.

References

1. R. D. Allen, G. B. David, and G. Nomarski, "The Zeiss-Nomarski differential equipment for transmitted light microscopy," *Z. Wiss Mikrosk* **69**(4), 193–221 (1969).
2. M. Pluta, *Advanced Light Microscopy. Vol. 2: Specialized Methods*, Elsevier Science Publishing, New York (1989).
3. S. Inoue, "Ultrathin optical sectioning and dynamic volume investigation with conventional light microscopy," Chapter 17 in *Three-Dimensional Confocal Microscopy: Volume Investigation of Biological Systems*, J. Stevens, L. Mills, and J. Trogadis, Eds., pp. 397–419, Academic Press, San Diego, CA (1994).
4. M. Born and E. Wolf, *Principles of Optics*, 7th ed., Cambridge University Press, Cambridge, England (2002).
5. P. S. Hauge, "Recent developments in instrumentation in ellipsometry," *Surf. Sci.* **96**, 108–140 (1980).
6. G. Mei and R. Oldenbourg, "Fast imaging polarimetry with precision universal compensator," in *Polarization Analysis and Measurement II*, D. H. Goldstein and D. B. Chenault, Eds., *Proc. SPIE* **2265**, 29–39 (1994).
7. T. Yamaguchi and H. Hasunuma, "A quick response recording ellipsometer," *Sci. Light (Tokyo)* **16**(1), 64–71 (1967).
8. R. M. A. Azzam and N. M. Bashara, *Ellipsometry and Polarized Light*, Elsevier, Amsterdam (1987).
9. M. Noguchi, T. Ishikawa, M. Ohno, and S. Tachihara, "Measurement of 2-D birefringence distribution," in *International Symposium on Optical Fabrication, Testing, and Surface Evaluation*, J. Tsujiuchi, Ed., *Proc. SPIE* **1720**, 367–378 (1992).

10. M. Shribak and R. Oldenbourg, "Sensitive measurements of two-dimensional birefringence distributions using near-circularly polarized beam," in *Polarization Analysis, Measurement, and Remote Sensing V*, D. H. Goldstein and D. B. Chenault, Eds., *Proc. SPIE* **4819**, 56–67 (2002).
11. A. M. Glazer and J. Cosier, "Method and apparatus for indicating optical anisotropy," U.K. Patent Application No. 2310925 (1997).
12. M. Shribak and R. Oldenbourg, "Retardance measurement system and method," U.S. Patent No. 7,202,950 (2007).
13. M. Shribak, "Orientation-independent differential interference contrast microscopy technique and device," U.S. Patent Application No. 2005/0152030 (2002).
14. M. Shribak and S. Inoué, "Orientation-independent differential interference contrast microscopy," *Appl. Opt.* **45**, 460–469 (2006).
15. B. Heise, A. Sonnleitner, and E. P. Klement, "DIC image reconstruction on large cell scans," *Microsc. Res. Tech.* **66**, 312–320 (2005).
16. C. Preza, "Rotational-diversity phase estimation from differential-interference-contrast microscopy images," *J. Opt. Soc. Am. A* **17**, 415–424 (2000).
17. M. R. Arnison, K. G. Larkin, C. J. R. Sheppard, N. I. Smith, and C. J. Cogswell, "Linear phase imaging using differential interference contrast microscopy," *J. Microsc.* **214**(Pt 1), 7–12 (2004).
18. F. Kagalwala and T. Kanade, "Reconstructing specimens using DIC microscope images," *IEEE Trans. Syst., Man, Cybern., Part B: Cybern.* **33**, 728–737 (2003).
19. T. J. Holmes, S. Bhattacharyya, J. A. Cooper, D. Hanzel, V. Krishnamurthi, W. Lin, B. Roysam, D. H. Szarowski, and J. N. Turner, "Light microscopic images reconstructed by maximum likelihood deconvolution", in *Handbook of Biological Confocal Microscopy*, James B. Pawley, Ed., pp. 389–402, Plenum Press, New York (1995).
20. D. Biggs and M. Andrews, "Acceleration of iterative image restoration algorithms," *Appl. Opt.* **36**, 1766–1775 (1997).
21. M. Shribak and R. Oldenbourg, "Technique for fast and sensitive measurements of two-dimensional birefringence distribution," *Appl. Opt.* **42**, 3009–3017 (2003).
22. E. D. Salmon and P. Tran, "High-resolution video-enhanced differential interference contrast light microscopy," Chapter 14 in *Digital Microscopy: A Second Edition of Video Microscopy*, G. Sluder and D. E. Wolf, Eds., pp. 289–318, Elsevier Academic Press, Amsterdam (2003).
23. D. C. France, V. Baru, M. Shribak, S. Inoué, S. McCutcheon, H. E. Buhse, and P. T. Matsudaira, "A centrin-based cellular spring that generates nNs of force", in *American Society for Cell Biology 45th Annual Meeting*, Abstracts CD, p. 73a (2005).